Regge phenomenology in π^0 and η photoproduction

V. L. Kashevarov,* M. Ostrick,† and L. Tiator‡

Institut für Kernphysik, Johannes Gutenberg-Universität Mainz, D-55099 Mainz, Germany

(Received 23 June 2017; revised manuscript received 16 August 2017; published 20 September 2017)

The $\gamma N \to \pi^0 N$ and $\gamma N \to \eta N$ reactions at photon beam energies above 4 GeV are investigated within Regge models. The models include t-channel exchanges of vector (ρ and ω) and axial-vector (b_1 and h_1) mesons. Moreover, Regge cuts of $\rho\mathbb{P}$, ρf_2, $\omega\mathbb{P}$, and ωf_2 are investigated. A good description of differential cross sections and polarization observables at photon beam energies from 4 to 15 GeV can be achieved.

DOI: 10.1103/PhysRevC.96.035207

I. INTRODUCTION

Meson photo- and electroproduction processes are closely related to the long-range structure and dynamics of hadrons. The phenomenology of these reactions changes at center of mass energies of about $W \approx 3$ GeV, roughly separating resonance and continuum regions.

Below $W \approx 3$ GeV, which corresponds to photon beam energies below $E_\gamma \approx 4$ GeV, the reaction dynamics is characterized by the excitation of individual s-channel baryon resonances with definite quantum numbers on top of a smooth, nonresonant background. Within the last two decades, new data on photoinduced meson production has become the major source of information for baryon spectroscopy. At the electron accelerator labs ELectron Stretcher Accelerator (ELSA), Thomas Jefferson National Accelerator Facility (JLab), and Mainz Microtron extensive developments in beam and target polarization techniques have been undertaken, and an enormous amount of data with different types of polarization has been obtained, especially for π, η, and K photoproduction [1]. Above this resonance region, at $W \gtrsim 3$ GeV, the reaction dynamics changes and can be described most effectively by particle (Reggeon) exchanges in the crossed t channel [2]. Experimental data on π and η photoproduction in this high-energy region were mainly measured in the 1970s at DESY [3–5] and Stanford Linear Accelerator Center (SLAC) [6], but only a limited amount of target and recoil polarization data is available. Only recently, the new GlueX experiment in Hall D at JLab started data taking, and first results on differential cross sections with a linearly polarized photon beam at $E_\gamma = 8.7$ GeV were already obtained [7].

The resonance and the continuum regions are, of course, not independent from each other but analytically connected via dispersion relations [8–11] or finite energy sum rules [12–14]. The motivation for this study is therefore twofold. First, with a view to new results on unpolarized cross sections and photon beam asymmetries expected from GlueX in the next years, we want to obtain a deeper understanding of the high-energy Regge phenomenology.

Second, we consider a good description of the high-energy data as an important prerequisite for a high-quality baryon resonance analysis at lower energies. In particular, in η, η', and K photoproduction a good knowledge about Regge contributions to nonresonant background amplitudes is crucial for a reliable extraction of resonance parameters.

The main features of our models are Regge trajectories from ω and ρ vector mesons and Regge cuts arising from the exchange of two Reggeons. We compare different approaches to available high-energy data for π^0 and η photoproduction at laboratory energies above 4 GeV. We show that particular polarization observables, such as photon beam and target asymmetries or recoil polarization, are crucial to distinguish between the different models.

This paper is organized as follows. In Sec. II we briefly introduce kinematics, polarization observables, and photoproduction amplitudes. In Sec. III we compare different Regge approaches with Regge poles and Regge cuts and discuss the various trajectories. In Sec. IV we compare different models to high-energy data of π^0 and η photoproduction for unpolarized cross sections and polarization observables.

II. KINEMATICS, OBSERVABLES, AND AMPLITUDES

A. Kinematics

Let us first define the kinematics of π and η photoproduction reactions on a nucleon,

$$\gamma(k) + N(p_i) \to \pi/\eta(q) + N'(p_f), \tag{1}$$

where the variables in brackets denote the four-momenta of the participating particles. The familiar Mandelstam variables are

$$s = (p_i + k)^2, \quad t = (q - k)^2, \quad u = (p_i - q)^2, \tag{2}$$

where the sum of the Mandelstam variables is given by the sum of the external masses. The crossing symmetrical variable ν is related to the photon laboratory energy $E_\gamma^{\rm lab}$ by

$$\nu = \frac{(s-u)}{4M_N} = E_\gamma^{\rm lab} + \frac{t-\mu^2}{4M_N}, \tag{3}$$

where M_N and μ are nucleon and meson masses (π or η), respectively.

B. Observables

In photoproduction of pseudoscalar mesons a total of 16 polarization observables can be measured, which include the

*kashev@kph.uni-mainz.de

†ostrick@kph.uni-mainz.de

‡tiator@uni-mainz.de

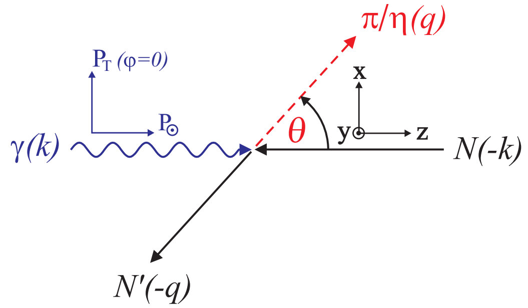

FIG. 1. Kinematics for π^0 or η photoproduction and frames for beam and target polarization.

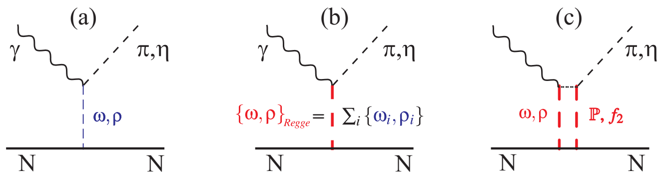

FIG. 2. t-channel contributions to η photoproduction from single poles (a), Regge poles (b), and Regge cuts (c). An example for ρ and ω meson exchange and $\mathbb{P}$ and f_2 mesons for rescattering of two Reggeons.

unpolarized cross section, 3 single-polarization and 12 double-polarization observables. By considering only beam and target polarization, the cross section depends on 8 observables, which can be separated by circular, $P_\odot$, and linear, P_T, photon beam polarization and the three components P_x, P_y, P_z of the target polarization vector:

$$\begin{aligned}\frac{d\sigma}{d\Omega} = \sigma_0\{&1 - P_T\Sigma\cos 2\varphi\\ &+ P_x(-P_T H\sin 2\varphi + P_\odot F)\\ &- P_y(-T + P_T P\cos 2\varphi)\\ &- P_z(-P_T G\sin 2\varphi + P_\odot E)\}.\end{aligned} \tag{4}$$

The z axis is pointing into the direction of the incoming photon. The $\hat{y}$ direction is perpendicular to the reaction plane, $\hat{y} = \hat{z}\times\hat{q}$, defined by the incoming photon and the direction of the outgoing meson $\hat{q}$. The x axis is given by $\hat{x} = \hat{y}\times\hat{z}$. The orientation of the linear polarization vector of the photon beam relative to the production plane is given by the angle φ; see Fig. 1. Expressions of the polarization observables in terms of amplitudes are given in the appendixes.

C. Invariant amplitudes and fixed-*t* dispersion relations

The electromagnetic current for pseudoscalar meson photoproduction can be expressed in terms of four invariant amplitudes $A_i(\nu,t)$ [15],

$$J^\mu = \sum_{i=1}^{4} A_i(\nu,t) M_i^\mu, \tag{5}$$

with the gauge-invariant four-vectors M_i^μ given by

$$\begin{aligned}M_1^\mu &= -\tfrac{1}{2} i\gamma_5(\gamma^\mu k\!\!\!/ - k\!\!\!/\gamma^\mu),\\ M_2^\mu &= 2i\gamma_5\left[P^\mu k\cdot\left(q-\tfrac{1}{2}k\right) - \left(q-\tfrac{1}{2}k\right)^\mu k\cdot P\right],\\ M_3^\mu &= -i\gamma_5(\gamma^\mu k\cdot q - k\!\!\!/ q^\mu),\\ M_4^\mu &= -2i\gamma_5(\gamma^\mu k\cdot P - k\!\!\!/ P^\mu) - 2M_N M_1^\mu,\end{aligned} \tag{6}$$

where $P^\mu = (p_i^\mu + p_f^\mu)/2$.

The invariant amplitudes $A_i(\nu,t)$ have definite crossing symmetry and satisfy dispersion relations at fixed t,

$$\mathrm{Re}A_i(\nu,t) = A_i^{\mathrm{pole}}(\nu,t) + \frac{2}{\pi}\,\mathcal{P}\int_{\nu_{\mathrm{thr}}}^{\infty} d\nu'\,\frac{\nu'\,\mathrm{Im}A_i(\nu',t)}{\nu'^2-\nu^2}, \tag{7}$$

for the crossing-even amplitudes, $A_{1,2,4}$, and

$$\mathrm{Re}A_3(\nu,t) = A_3^{\mathrm{pole}}(\nu,t) + \frac{2\nu}{\pi}\,\mathcal{P}\int_{\nu_{\mathrm{thr}}}^{\infty} d\nu'\,\frac{\mathrm{Im}A_3(\nu',t)}{\nu'^2-\nu^2} \tag{8}$$

for the crossing-odd amplitude A_3 [10].

III. *t*-CHANNEL EXCHANGES

A. Vector and axial-vector poles in the *t* channel

The amplitudes of pseudoscalar meson photoproduction typically contain contributions from nucleon resonance excitations and a nonresonant background from Born terms and t-channel meson exchanges. In the current approach we want to consider only amplitudes at high energies beyond the nucleon resonance region. Furthermore, we neglect Born terms, which are practically zero for η photoproduction [16]. Also in π^0 photoproduction they only play a minor role at forward angles.

We concentrate on t-channel contributions and will first consider the exchange of vector and axial-vector mesons in terms of single-pole Feynman diagrams; see Fig. 2(a) as an example for ρ and ω meson exchange.

Expressed in terms of invariant amplitudes A_i, these t-channel Feynman diagrams obtain the simple form

$$A_1(t) = \frac{e\,\lambda_V\,g_V^{\mathfrak{t}}}{2\mu M_N}\,\frac{t}{t-M_V^2}, \tag{9}$$

$$A_2'(t) = -\frac{e\,\lambda_A\,g_A^{\mathfrak{t}}}{2\mu M_N}\,\frac{t}{t-M_A^2}, \tag{10}$$

$$A_3(t) = \frac{e\,\lambda_A\,g_A^{v}}{\mu}\,\frac{1}{t-M_A^2}, \tag{11}$$

$$A_4(t) = \frac{-e\,\lambda_V\,g_V^{v}}{\mu}\,\frac{1}{t-M_V^2}, \tag{12}$$

where $\lambda_{V(A)}$ denotes the electromagnetic coupling of the vector (V) or axial (A) vector mesons with masses $M_{V(A)}$. The constants $g_{V(A)}^{v(\mathfrak{t})}$ denote their vector (v) or tensor ($\mathfrak{t}$) couplings to the nucleon. To separate the vector and tensor contributions from individual mesons, we followed Ref. [14] and introduced the amplitude

$$A_2'(t) = A_1(t) + t\,A_2(t), \tag{13}$$

which has only contributions from the tensor coupling of an axial-vector exchange.

TABLE I. Isospin I, G-parity, spin J, parity P, and charge conjugation C quantum numbers for pseudoscalar, vector, and axial-vector mesons.

	γ	π^0	η	$\rho(770)$	$\omega(782)$	$\phi(1020)$	$b_1(1235)$	$h_1(1170)$	$a_1(1260)$	$f_1(1285)$
I^G	0,1	1^-	0^+	1^+	0^-	0^-	1^+	0^-	1^-	0^+
J^{PC}	1^{--}	0^{-+}	0^{-+}	1^{--}	1^{--}	1^{--}	1^{+-}	1^{+-}	1^{++}	1^{++}

There are three vector mesons ρ, ω, ϕ and four axial vector mesons b_1, h_1, a_1, f_1 that could be used in our approach. The details on the quantum numbers are listed in Table I. For the nucleon vertex, the axial-vector coupling $\gamma^\mu\gamma_5$ is C-even and the pseudotensor coupling $\sigma^{\mu\nu}\gamma_5$ is C-odd [17]. Therefore, owing to charge conjugation conservation, the C-odd b_1 and h_1 mesons couple to the nucleon via the tensor coupling only and can contribute to the A_2 (A_2') amplitude [see Eqs. (10) and (13)], whereas C-even a_1 and f_1 mesons couple to the nucleon via the vector coupling only and, in principal, can contribute to the A_3 amplitude. However, the quantum numbers I^G should be equal to 0^- or 1^+ for π^0 and η photoproduction on the nucleon. Consequently, $a_1(I^G = 1^-)$ and $f_1(I^G = 0^+)$ are excluded in our case. The a_1 is a good candidate for charged-pion photoproduction and f_1 for the $\gamma p \to \rho^0 p$ channel [10]. Therefore, there is no candidate left among vector and axial-vector mesons which could contribute to A_3.

The ϕ meson could, in principle, contribute to A_1 and A_4. However, being practically a pure strange quark-antiquark state, a very small coupling to the nucleon is expected and it is commonly neglected in π^0 and η photoproduction.

The invariant amplitudes (9)–(12) contain only the product of electromagnetic and hadronic coupling constants. We have fixed one of them and determined the second one by the fit. In general, the values for the strong coupling constants g^v and g^t are not well known, especially for the axial-vector mesons. Results for these constants from different analyses and models are summarized in Ref. [18], Table IV. Therefore, in our present work, we fix the electromagnetic couplings $\lambda_{V(A)}$. For π^0 and η photoproduction they can be determined from the radiative widths $\Gamma_{V(A)}$ of the decays $V(A) \to \pi^0\gamma$ and $V(A) \to \eta\gamma$, respectively,

$$\Gamma_{V(A)} = \frac{\alpha\left(M^2_{V(A)} - \mu^2\right)^3}{24\, M^3_{V(A)}\, \mu^2}\, \lambda^2_{V(A)}, \tag{14}$$

where α is the fine-structure constant. For $\lambda_{V\pi^0\gamma}$ we used the decay widths $\Gamma_{\rho\to\pi^0\gamma} = 91.0$ keV and $\Gamma_{\omega\to\pi^0\gamma} = 703.0$ keV. In case of the η meson, we determined $\lambda_{V\eta\gamma}$ from $\Gamma_{\rho\to\eta\gamma} = 50.6$ keV and $\Gamma_{\omega\to\eta\gamma} = 3.9$ keV [19]. For the b_1 meson only the electromagnetic width for the charged decay $\Gamma_{b_1\to\pi^\pm\gamma} = 227$ keV is known [19]. We use this value to calculate λ_{b_1} for the neutral decay as well, because chiral unitary models predict practically the same electromagnetic couplings of the b_1 meson for both charged and neutral pion decays [20]. Unfortunately, there are no data for the decay $b_1 \to \eta\gamma$. In this case, we arbitrarily fixed $\lambda_{\eta\gamma} = 0.1$, which is close to the value obtained for the $\pi\gamma$ decay. All electromagnetic coupling constants for the ρ, ω, and b_1 mesons used in the present work are listed in Table IV. For the contribution of the h_1 meson we follow Ref. [14], which suggests a fraction of 2/3 of the b_1 contribution.

B. Regge trajectories and t-channel Regge amplitudes

Mesons fall into linear trajectories when their spin is plotted against the squared meson masses (Chew-Frautschi plot). These Regge trajectories are usually parametrized as

$$\alpha(t) = \alpha_0 + \alpha' t; \tag{15}$$

see, e.g., Ref. [21]. Examples of such trajectories are shown in Fig. 3(a).

It can be assumed that in photoproduction reactions not only single mesons but whole Regge trajectories are exchanged in the t channel, as illustrated in Fig. 2(b). In our models we include the ρ, ω, ϕ, and b_1 trajectories shown in Fig. 3(a). The trajectory for the h_1 is assumed to be the same as for the b_1 furthermore, trajectories for tensor mesons ρ_2 and ω_2 are shown in the same plot. These mesons, assuming the same masses for both, were predicted in a relativized quark model [24] for two states: $J^{PC} = 2^{--}$ with mass of 1.7 GeV and $J^{PC} = 4^{--}$ with mass of 2.34 GeV. The trajectory drawn through these two points is shown by the magenta line. According to their quantum numbers, the ρ_2 and ω_2 could be good candidates for the A_3 amplitude in π^0 and η photoproduction. However, there is no clear experimental evidence for the existence of these states. They were found in a partial wave analysis of Refs. [22,23] and result in much steeper trajectories, which are shown in Fig. 3(a) by the dashed magenta line for the ρ_2 and dash-dotted magenta line for the ω_2.

Technically, the t-channel exchange of Regge trajectories is done by replacing the single meson propagator by the expression

$$\frac{1}{t - M^2} \Rightarrow \left(\frac{s}{s_0}\right)^{\alpha(t)-1} \frac{\pi\,\alpha'}{\sin[\pi\alpha(t)]}\, \frac{\mathcal{S} + e^{-i\pi\alpha(t)}}{2}\, \frac{1}{\Gamma[\alpha(t)]}, \tag{16}$$

where M is the mass of the Reggeon, $\mathcal{S}$ is the signature of the Regge trajectory, and s_0 is a mass scale factor, commonly set to 1 GeV^2. The Γ function $\Gamma[\alpha(t)]$ is introduced to suppress additional poles of the propagator. The signature $\mathcal{S}$ is determined as $\mathcal{S} = (-1)^J$ for bosons and $\mathcal{S} = (-1)^{J+1/2}$ for fermions. So $\mathcal{S} = -1$ for the vector and axial-vector mesons, and $\mathcal{S} = +1$ for tensor mesons. If $\mathcal{S} = -1$ and $\alpha(t) = 0$, then both real and imaginary parts vanish. This results in a characteristic dip of differential cross sections of $\gamma p \to \pi^0 p$ and $\gamma p \to \eta p$ reactions at $t \approx -0.5$ GeV^2, which is not observed in experimental data; see Fig. 4.

To avoid problems with the dip at $\alpha(t) = 0$, different approaches have been developed; see, for example,

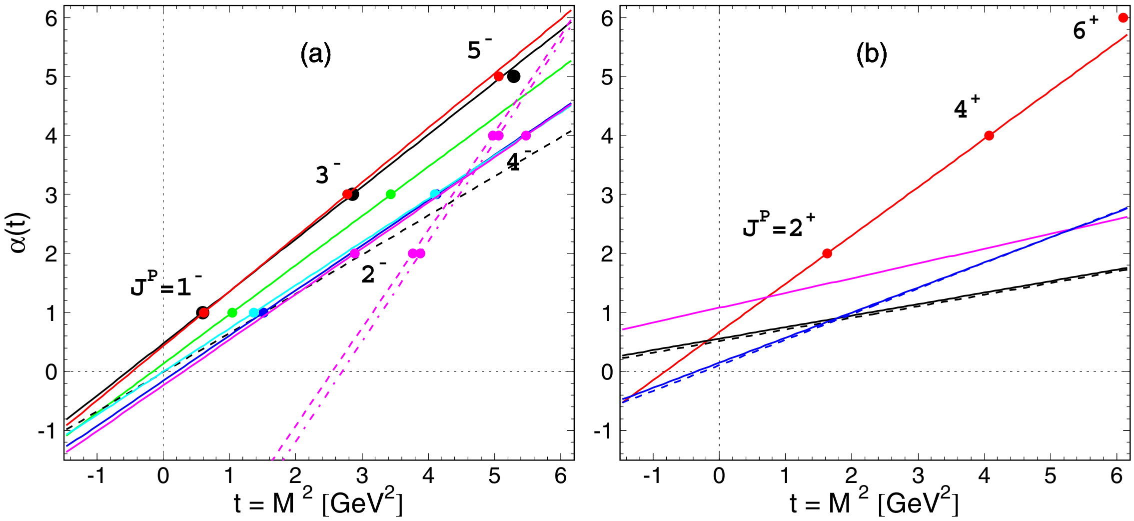

FIG. 3. Regge trajectories: (a) ρ, black; ω, red; ϕ, blue; b_1 and h_1, green; ρ_2 and ω_2, magenta (dashed and dash-dotted magenta lines are ρ_2 and ω_2 of Refs. [22,23]); (b) f_2, red; $\mathbb{P}$, magenta; ρf_2, black solid; ωf_2, blue dashed; $\rho\mathbb{P}$, black solid; $\omega\mathbb{P}$, black dashed.

Refs. [14,16,25–29]. Here we focus on two of them, which are described in the following sections.

C. Regge cuts

Regge cuts were first considered in the early work of Refs. [25,26,30], where their important role was shown to fill in the dip in the differential cross sections of π^0 and η photoproduction. A full discussion of Regge cuts can be found in Ref. [31]. In 2016 Donnachie and Kalashnikova [28] revisited the Regge cuts and developed a new approach, where in addition to Regge trajectories of ρ, ω, and b_1 exchange, Regge cuts from rescattering $\rho\mathbb{P}$,ρf_2 and $\omega\mathbb{P}$,ωf_2 also were added, where $\mathbb{P}$ is the Pomeron with quantum numbers of the vacuum $0^+(0^{++})$ and f_2 is a tensor meson with quantum numbers $0^+(2^{++})$. These Regge cuts can be considered as contracted box diagrams, where two particles are exchanged; see Fig. 3(c).

The exchange of two Reggeons with linear trajectories

$$\alpha_i(t) = \alpha_i(0) + \alpha_i' t, \quad i = 1,2, \tag{17}$$

yields a cut with a linear trajectory $\alpha_c(t)$ [30],

$$\alpha_c(t) = \alpha_c(0) + \alpha_c' \, t, \tag{18}$$

where

$$\alpha_c(0) = \alpha_1(0) + \alpha_2(0) - 1,$$
$$\alpha_c' = \frac{\alpha_1'\alpha_2'}{\alpha_1' + \alpha_2'}. \tag{19}$$

The trajectories for f_2 and $\mathbb{P}$ are shown in Fig. 3(b) together with four cut trajectories $\rho\mathbb{P}$, $\omega\mathbb{P}$ (black solid and dashed lines) and ρf_2, ωf_2 (blue solid and dashed lines) calculated by Eqs. (17)–(19). Parameters of the Reggeon and cut trajectories used in the present work are collected in Table II.

All four Regge cuts can contribute to vector and axial-vector exchanges and can be written in the following form:

$$D_{\rm cut} = \left(\frac{s}{s_0}\right)^{\alpha_c(t)-1} e^{-i\pi\alpha_c(t)/2}\, e^{d_c t}. \tag{20}$$

In total, the vector meson propagators are replaced with

$$D_V = D_V + c_{V\mathbb{P}} D_{V\mathbb{P}} + c_{Vf_2} D_{Vf_2}, \quad V = \rho,\omega, \tag{21}$$

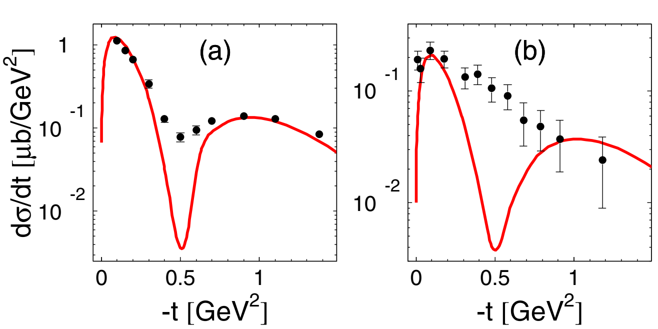

FIG. 4. The differential cross sections of $\gamma p \to \pi^0 p$ (a) and $\gamma p \to \eta p$ (b) reactions at $E_\gamma = 6$ GeV. Experimental data are from Ref. [6] (a) and Ref. [3] (b). The solid line is a calculation with ρ and ω exchange in the t channel.

TABLE II. The Reggeon and cut trajectories used in the present work.

Reggeon or cut	$\alpha(t)$
ρ	$0.477 + 0.885t$
ω	$0.434 + 0.923t$
$b_1, h_1,$	$-0.013 + 0.664t$
ρ_2, ω_2	$-0.235 + 0.774t$
$f_2,$	$0.671 + 0.817t$
$\mathbb{P}$	$1.08 + 0.25t$
ρf_2	$0.148 + 0.425t$
ωf_2	$0.106 + 0.436t$
$\rho\mathbb{P}$	$0.557 + 0.195t$
$\omega\mathbb{P}$	$0.514 + 0.197t$

TABLE III. Vector and axial-vector contributions to invariant amplitudes.

η	J^P	Dirac coupling	Invariant amplitudes	Reggeons and cuts
Natural	$1^-,3^-,\ldots$	$g_V^v\gamma^\mu$	A_4	$\rho,\omega,\rho\mathbb{P},\omega\mathbb{P},\rho f_2,\omega f_2$
Natural	$1^-,3^-,\ldots$	$g_V^t\sigma^{\mu\nu}$	A_1	$\rho,\omega,\rho\mathbb{P},\omega\mathbb{P},\rho f_2,\omega f_2$
Unnatural	$2^-,4^-,\ldots$	$g_A^v\gamma^\mu\gamma_5$	A_3	$\rho_2,\omega_2,\rho f_2,\omega f_2$
Unnatural	$1^+,3^+,\ldots$	$g_A^t\sigma^{\mu\nu}\gamma_5$	A_2'	$b_1,h_1,\rho f_2,\omega f_2$

and the axial-vector meson propagators are replaced with

$$D_A = D_A + \sum_{V=\rho,\omega} (\tilde{c}_{V\mathbb{P}} D_{V\mathbb{P}} + \tilde{c}_{Vf_2} D_{Vf_2}), \quad A = b_1,h_1, \tag{22}$$

where the coefficients $c_{V\mathbb{P}},c_{Vf_2}$ are for natural parity cuts and $\tilde{c}_{V\mathbb{P}},\tilde{c}_{Vf_2}$ for unnatural parity cuts and are obtained by a fit to the data.

In detail, the invariant amplitudes will be changed in the following way:

$$\begin{aligned}
\lambda_\rho g_\rho^{v,t}\,\frac{1}{t-M_\rho^2} &\to \lambda_\rho g_\rho^{v,t}[D_\rho(s,t) + c_{\rho\mathbb{P}} D_{\rho\mathbb{P}}(s,t) \\
&\quad + c_{\rho f} D_{\rho f}(s,t)], \\
\lambda_\omega g_\omega^{v,t}\,\frac{1}{t-M_\omega^2} &\to \lambda_\omega g_\omega^{v,t}[D_\omega(s,t) + c_{\omega\mathbb{P}}\, D_{\omega\mathbb{P}}(s,t) \\
&\quad + c_{\omega f} D_{\omega f}(s,t)], \\
\lambda_{b_1} g_{b_1}^{t}\,\frac{1}{t-M_{b_1}^2} &\to \lambda_{b_1} g_{b_1}^{t} D_{b_1}(s,t) + \lambda_\rho g_\rho^{t}\,[\tilde{c}_{\rho\mathbb{P}} D_{\rho\mathbb{P}}(s,t) \\
&\quad + \tilde{c}_{\rho f_2} D_{\rho f_2}(s,t)] + \lambda_\omega g_\omega^{t}\,[\tilde{c}_{\omega\mathbb{P}} D_{\omega\mathbb{P}}(s,t) \\
&\quad + \tilde{c}_{\omega f_2} D_{\omega f_2}(s,t)].
\end{aligned} \tag{23}$$

In practical calculations, it turns out that the axial-vector Regge pole contributions, proportional to D_A, can be neglected, but the axial vector Regge cuts arising from ρ and ω together with $\mathbb{P}$ and f_2 are very important, in particular for polarization observables, as the photon beam asymmetry Σ.

The Regge cuts also allow us to describe a long standing problem of suitable candidates for an A_3 amplitude: ρf_2 and ωf_2 satisfy all conservation law requirements. In Table III details of the invariant amplitude structure of the t-channel exchanges are given. Here, η is a naturality, determined as $\eta = P(-1)^J$. For the $\rho\mathbb{P}$ and $\omega\mathbb{P}$ cuts, $\eta = +1$, and these cuts do not contribute to the A_3 amplitude. Therefore, we set the coefficients $\tilde{c}_{\rho\mathbb{P}}$ and $\tilde{c}_{\omega\mathbb{P}}$ in Eq. (23) equal to zero.

D. Regge amplitudes and fixed-t dispersion relations

The formulation of Regge amplitudes as given in the Sec. III.B does not satisfy fixed-t dispersion relations. The reason is mainly given by the ansatz in Eq. (16), where the energy dependence is proportional to $s^{[\alpha(t)-1]}$, violating crossing symmetry. As an alternative ansatz we also used the parametrization of Ref. [14] [Joint Physics Analysis Center (JPAC) model]:

$$D_{V,A} = -\beta_i(t)\,\frac{\pi\,\alpha'_{V,A}(e^{-i\pi\alpha_{V,A}(t)}-1)}{2\sin[\pi\alpha_{V,A}(t)]}\big({r_i}^{V,A}\nu\big)^{\alpha_{V,A}(t)-1}. \tag{24}$$

Here the Mandelstam variable s is replaced with the crossing variable ν, and the Γ function in the denominator of Eq. (16) is replaced with a more general residue $\beta_i(t)$, where $i = 1,2,3,4$ is the index of the invariant amplitudes. ${r_i}^{V,A}$ are scale parameters of dimension GeV^{-1}. Each exchange, V or A, has its own scale parameter.

In Ref. [14] residues for $V = \rho,\omega$ and $A = b,h$ are given,

$$\beta_1^V(t) = g_1^V t\,\frac{-\pi\alpha'^V}{2}\,\frac{1}{\Gamma[\alpha^V(t)+1]}, \tag{25}$$

$$\beta_4^V(t) = g_4^V\,\frac{-\pi\alpha'^V}{2}\,\frac{1}{\Gamma[\alpha^V(t)]}, \tag{26}$$

$$\beta_2'^A(t) = g_2^A t\,\frac{-\pi\alpha'^A}{2}\,\frac{1}{\Gamma[\alpha^A(t)+1]}, \tag{27}$$

where the prime in β_2' denotes the fact that this is the A_2' residue, which explains the factor of t. The factor $-\pi\alpha'/2$ ensures the correct on-shell couplings. The functions $1/\Gamma(\alpha+1)$ and $1/\Gamma(\alpha)$ are both equal to 1 at the pole $\alpha = 1$; however, they differ in the physical region.

As possible candidates for the A_3 amplitude, tensor mesons ρ_2 and ω_2 were suggested in Ref. [14]. The signature for the tensor mesons is equal to $+1$, so we use a parametrization for the propagator,

$$D_T = -\beta_3(t)\,\frac{\pi\,\alpha'_T(e^{-i\pi\alpha_T(t)}+1)}{2\sin[\pi\alpha_T(t)]}\,\big({r_i}^{V,A}\nu\big)^{\alpha_T(t)-1}, \tag{28}$$

with the residue

$$\beta_3^T(t) = g_3^T\,\frac{-\pi\alpha'^T}{2}\,\frac{1}{\Gamma[\alpha^T(t)]}, \tag{29}$$

where a symbol T denotes the tensor meson, ρ_2 or ω_2. Parameters of the trajectories of these mesons are shown in Table II. Furthermore, we also assume the same contributions to A_3 from both mesons.

TABLE IV. Coupling constants for π^0 and η photoproduction used in Fit I as fixed values.

Reggeon	$\lambda_{\pi^0\gamma}$	$\lambda_{\eta\gamma}$	g^v	g^t
ρ	0.115	0.910	2.7	4.2
ω	0.310	0.246	14.2	0
b_1	0.091	0.1	0	-7.6

IV. RESULTS

We have used the Regge cut and JPAC models for a fit to the available data for $\gamma p \to \pi^0 p$ and $\gamma p \to \eta p$ at $E_\gamma \geqslant 4$ GeV. The electromagnetic coupling constants for the ρ, ω, and b_1 mesons were fixed according to Table IV. The best fit using Regge cuts is called Solution I.

As the first step in fits with the JPAC approach, we reproduced exactly the results from Ref. [14] for the differential

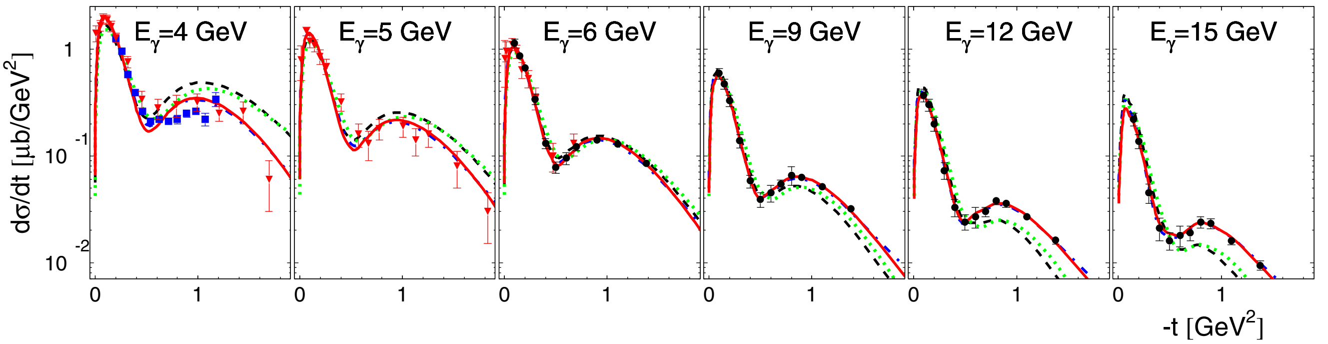

FIG. 5. Differential cross sections for $\gamma p \to \pi^0 p$. The solid red, dashed black, dash-dotted blue (coincide mostly with red curves), and dotted green lines are our Solutions I, II, III, and IV, respectively. Data are from SLAC [6] (black circles) and from DESY, [5] (red triangles) and [4] (blue squares).

cross section of the $\gamma p \to \eta p$ reaction. We then added the tensor mesons ρ_2 and ω_2 with electromagnetic couplings fixed to 1 and fitted the model to all available data in π^0 and η production. This result is called Solution II.

A. Results on π^0 photoproduction

In the fits we have used the experimental data for the differential cross sections $d\sigma/dt$ from DESY at $E_\gamma = 4$ GeV [4] and $E_\gamma = 4$,5, and 5.8 GeV [5], and SLAC [6] at $E_\gamma = 6$,9,12, and 15 GeV; the polarized-beam asymmetry Σ from SLAC [6] at $E_\gamma = 4$,6, and 10 GeV and GlueX [7] at $E_\gamma = 8.7$ GeV; the target asymmetry T from Daresbury [32] and DESY [33], both at $E_\gamma = 4$ GeV; the recoil polarization observable P from Cambridge Electron Accelerator (CEA) [34] at $E_\gamma = 4.1$–6.3 GeV; the differential cross-section ratio of neutrons and protons, R_{np} for π^0 photoproduction at $E_\gamma = 4$ GeV [35,36] and $E_\gamma = 4.7$ and 8.2 GeV [37].

The fit results, together with the experimental data, are presented in Fig. 5 for the differential cross sections, in Fig. 6 for the polarization observables, and in Fig. 7 for the ratio R_{np}. The data for the recoil polarization observable P are divided in two groups and are shown on panel $E_\gamma = 5$ GeV for $E_\gamma = 4.5$–5.5 GeV and on panel $E_\gamma = 6$ GeV for $E_\gamma = 5.5$–6.3 GeV. The best fit with reduced $\chi^2_{\rm red} = 1.46$ using the Regge cut model is shown by the red lines (Solution I). This solution describes practically all experimental data except the beam asymmetry Σ at $E_\gamma = 8.7$ GeV [7] very well. The old data from SLAC [6] for Σ at $E_\gamma = 6$ and 10 GeV show a clear dip at $t = -0.5$ GeV^2. Surprisingly, such a structure is missing for the intermediate energy of 8.7 GeV in the new GlueX data [7]. Therefore, we also performed an alternative fit using the Regge cut model without the old polarization data and obtained Solution III with $\chi^2_{\rm red} = 0.92$, which is shown in Figs. 5, 6, and 7 by the dash-dotted blue line. This solution

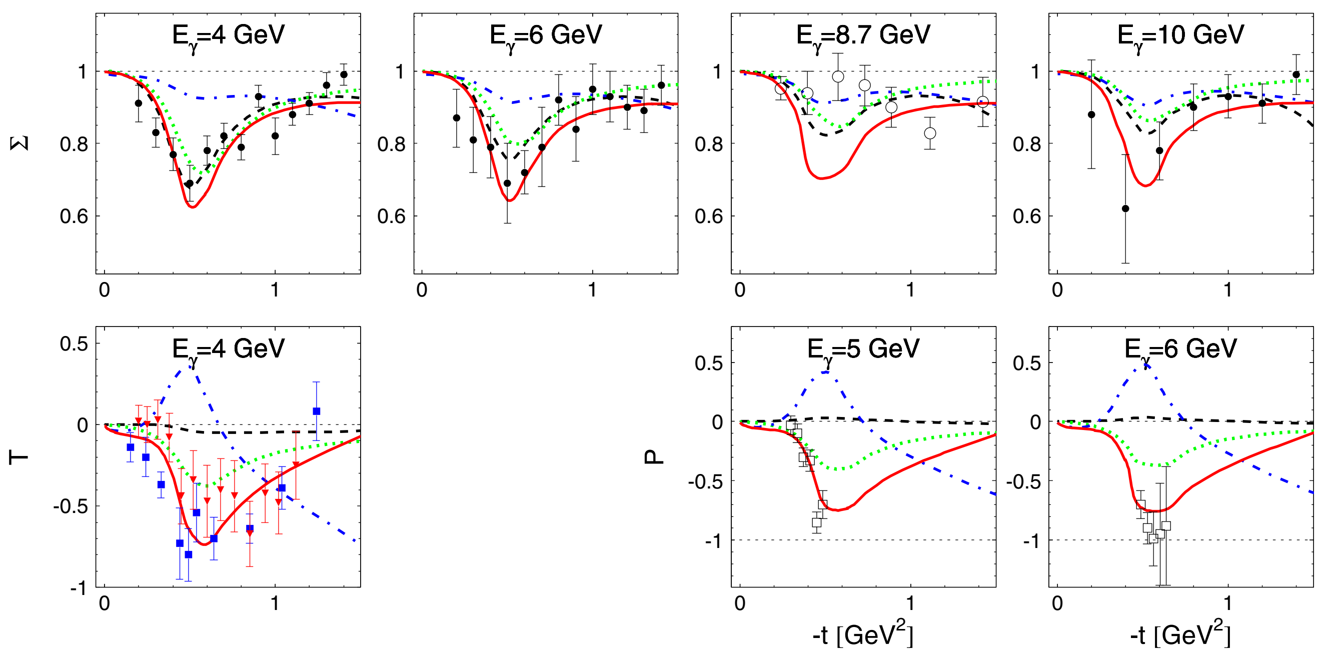

FIG. 6. Polarization observables Σ, T, and P for $\gamma p \to \pi^0 p$. The notation of the lines is the same as in Fig. 5. Data: SLAC [6] (black disks), GlueX-17 [7] (black open circles), Daresbury [32] (red triangles), DESY [33] (blue solid squares), CEA [34] (blue open squares).

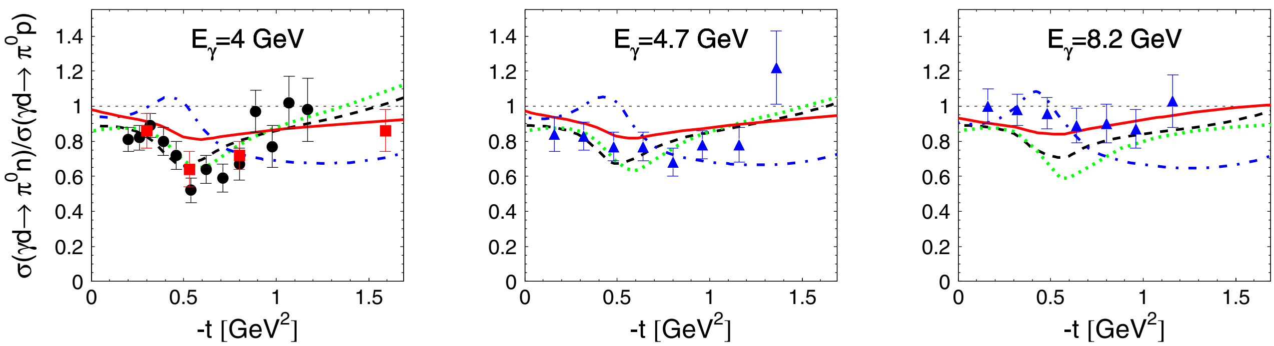

FIG. 7. Ratio of differential cross sections for π^0 photoproduction on neutrons and protons. The notation of the lines is the same as in Fig. 5. Data: DESY [35] (black circles), CEA [36] (red squares), and Cornell [37] (blue triangles).

can describe the GlueX data quite well, but it is absolutely wrong for T and P and also underestimates the old data for Σ. Therefore, we conclude that a strong energy dependence of the beam asymmetry between 6 and 10 GeV, as suggested by the GlueX data, cannot be described within our model without adding additional dynamics. There is also some disagreement between the data and Solution I for the differential cross sections at $E_\gamma = 4$ GeV; see Figs. 5 and 7. This energy corresponds to the center-of-mass energy $W = 2.9$ GeV, which is close to the resonance region. Probably, tails from the resonance contributions still show up in this energy region for π^0 photoproduction and should be taken into account.

The central values of the fit parameters for Solutions I and III are shown in Table V together with associated uncertainties. Parameters without errors were fixed in the fits. The coefficients $\tilde{c}_{\rho\mathbb{P}}$ and $\tilde{c}_{\omega\mathbb{P}}$ are zero because the corresponding terms for the $\rho\mathbb{P}$ and $\omega\mathbb{P}$ cuts do not contribute to the A_3 amplitude; see Table III. There are also two parameters for the $\gamma p \to \eta p$ reaction that were fixed by empirical constraints: $d_{\omega\mathbb{P}} = d_{\rho\mathbb{P}}$ and $d_{\omega f_2} = d_{\rho f_2}$.

The best fit with the JPAC model has $\chi^2_{\rm red} = 5.59$ (Solution II); see black dashed lines in Figs. 5 and 6. It describes well the shape of the differential cross sections but has the wrong energy dependence after the dip location, $-t > 0.4$ GeV^2. Similar to the Regge cut solution, it does not describe the new GlueX data for Σ. Furthermore, the existing data on the polarization observables T and P cannot be described. The inclusion of the exotic tensor mesons ρ_2 and ω_2 did not improve our fits, and we did not consider them in our four solutions.

We then investigated the possibility of improving the fit by including the ϕ meson in the JPAC model even though small couplings to the nucleon can be expected as discussed above. The electromagnetic coupling constants $\lambda_{\phi\pi^0\gamma} = 0.018$ and $\lambda_{\phi\eta\gamma} = 0.38$ are obtained from the corresponding widths $\Gamma_{\phi\to\pi^0\gamma} = 5.4$ keV and $\Gamma_{\phi\to\eta\gamma} = 55.84$ keV [19] using Eq. (14). This Solution IV is shown in Figs. 5, 6, and 7 by the green dotted lines. We did not use ρ_2 and ω_2 for this fit because of their negligible contributions. Indeed, Solution IV describes the polarization observables T and P significantly better than Solution II. The hadronic vector $g^v = -4.3$ and tensor $g^t = -0.08$ coupling constants for ϕ meson were obtained from this fit, which we consider as reasonable. A comparison of $\chi^2_{\rm red}$ for the different solutions is shown in Table VI.

Table VII gives partial χ^2 divided by the number of the data points for each observable and each laboratory, for Solutions I and III.

B. Results on η photoproduction

The data set for the $\gamma p \to \eta p$ reaction at high energies is more limited than for π^0 photoproduction. For the fit, we have used the experimental data of the differential cross sections $d\sigma/dt$ from DESY [3] at $E_\gamma = 4$ and 6 GeV and Wilson Laboratory Synchrotron (WLS) [38] at $E_\gamma = 4$ and 8 GeV; for the polarized-beam asymmetry Σ from GlueX [7] at $E_\gamma = 8.7$ GeV; and for the target asymmetry T from Daresbury [39].

TABLE V. Parameter values obtained from Fit I and Fit III for π^0 and η photoproduction.

Solution	Reaction	$c_{\rho\mathbb{P}}$	$c_{\omega\mathbb{P}}$	$c_{\rho f_2}$	$c_{\omega f_2}$	$\tilde{c}_{\rho\mathbb{P}}$	$\tilde{c}_{\omega\mathbb{P}}$	$\tilde{c}_{\rho f_2}$	$\tilde{c}_{\omega f_2}$	$d_{\rho\mathbb{P}}$	$d_{\omega\mathbb{P}}$	$d_{\rho f_2}$	$d_{\omega f_2}$
I	$\gamma p \to \pi^0 p$	0.52	−0.06	0.72	2.98	0	0	−0.65	0.007	1.07	0.37	0.62	5.02
		±0.08	±0.01	±0.64	±0.49	—	—	±0.26	±0.1	±0.71	±0.14	±0.43	±0.77
I	$\gamma p \to \eta p$	−2.27	0.016	5.89	−5.96	0	0	−0.18	0.25	5.5	5.5	2.36	2.36
		±0.92	±0.09	±0.81	±0.83	—	—	±0.28	±0.37	±2.1	—	±0.19	—
III	$\gamma p \to \pi^0 p$	−0.49	0.23	1.08	2.25	0	0	0.24	0.08	0.66	9.9	0.001	4.16
		±0.09	±0.01	±0.84	±0.32	—	—	±0.31	±0.1	±0.16	±0.61	±0.87	±0.51
III	$\gamma p \to \eta p$	−2.59	−0.25	6.51	−5.77	0	0	−0.17	−0.13	5.5	5.5	2.49	2.49
		±0.83	±0.31	±0.79	±0.85	—	—	±0.33	±0.39	±4.4	—	±0.18	—

TABLE VI. Four solutions using different models and data sets shown in our analysis.

Solution	Line in figures	Model	Data set	$\chi^2_{\rm red}(\pi)$	$\chi^2_{\rm red}(\eta)$
I	Solid red	Regge cut	All	1.46	1.25
II	Dashed black	JPAC	All	5.59	2.73
III	Dashed-dotted blue	Regge cut	$d\sigma/dt$ + GlueX Σ	0.92	1.07
IV	Dotted green	JPAC+ϕ	All	4.17	1.86

Our fit results for the differential cross sections are presented in Fig. 8 and for the polarization observables Σ and T in Fig. 9. The data for $d\sigma/dt$ and Σ at $E_\gamma = 3$ GeV were not included in the fit because these are very close to the resonance region. However, the predictions of all our solutions can reproduce also these data quite well. Presumably, the influence of the resonances for η photoproduction is already negligible at these energies. Our extrapolation of the differential cross section to $E_\gamma = 3$ GeV is in good agreement with Ref. [43].

The best fit with $\chi^2_{\rm red} = 1.25$ using the Regge cut model is shown by the solid red line (Solution I). This solution well describes all experimental data including the beam asymmetry Σ at $E_\gamma = 8.7$ GeV [7]. The alternative fit without data for T, Solution III, also gives a good prediction for this observable.

Table VIII gives partial χ^2 divided by the number of the data points for each observable and each laboratory, similar to Table VII, but for η photoproduction.

The fit with the JPAC model has a $\chi^2_{\rm red} = 2.73$ (Solution II); see dashed black lines in Figs. 8 and 9. Similar as for π^0 photoproduction, it well describes the differential cross section and Σ, but contradicts the data for T. As in case of π^0 production, the inclusion of the ϕ meson (Solution IV), improves the description significantly at low t. However, a main drawback of Solution IV is a large overestimation of the total cross section at energies $E_\gamma > 2$ GeV. Therefore, this solution cannot be used as a nonresonant background for partial wave analyses in the resonance region.

C. Further results for high energies

From high-energy approximations of the observables the following relation between the target and recoil polarization to the photon beam asymmetry can be derived in a model-independent way (see appendixes):

$$|P - T| \leqslant 1 - \Sigma. \tag{30}$$

As the beam asymmetry Σ is almost unity, except in the neighborhood of the dip near $t = -0.5$ GeV^2, the polarization observables T and P should be almost equal. Any difference between T and P should be attributable to an interference between the A_2' and A_3 amplitudes at high energies; see Eqs. (C3) and (C4) in Appendix C. A comparison between T and P for Solutions I and II is shown in Fig. 10. Solution I for π^0 photoproduction verifies well this prediction. There is some visible difference between T and P for η photoproduction, but in this case no P data were included in the fit.

V. SUMMARY AND CONCLUSIONS

Photoproduction π^0 and η mesons on the nucleon at photon beam energies above 4 GeV was investigated within two different Regge model approaches. The models include t-channel exchange of vector (ρ and ω) and axial-vector (b_1 and h_1) mesons. Moreover, Regge cuts of $\rho\mathbb{P}$, ρf_2, $\omega\mathbb{P}$, and ωf_2 are used. Both models can describe differential cross sections and photon beam asymmetries Σ very well, except for a possible strong energy dependence of Σ in $\gamma p \to \pi^0 p$ between 6 and 10 GeV, as suggested by recent GlueX data. Within our approach we cannot find a solution that can simultaneously describe both the old polarization data and the new GlueX data.

The crossing-odd amplitude A_3 gets no contributions from dominant t-channel vector meson exchange terms. We found possible contributions from tensor meson exchanges and also from Regge cuts. All of them turn out to be rather small. The effect could be worked out in the difference between target and recoil polarizations, but from existing data in π^0 photoproduction no evidence can be seen.

Finally, with the present database only the Regge cut model (Solution I) is able to describe all other available polarization observables as well. However, because most data go back to the late 1960s and early 1970s, and, however, new data are in progress, a reliable conclusion cannot yet be drawn. For our applications in forthcoming baryon resonance analyses from pseudoscalar meson photoproduction data, we currently favor an extrapolation of Solution I to lower energies as a good description for the nonresonant background.

ACKNOWLEDGMENTS

We would like to thank V. Mathieu, J. Nys, and M. Vanderhaeghen for very fruitful discussions. This work was supported by the Deutsche Forschungsgemeinschaft (Grant No. SFB 1044).

APPENDIX A: OBSERVABLES IN TERMS OF CGLN AMPLITUDES

Here the polarization observables involving beam and target polarization are expressed by helicity amplitudes in the notation of Barker *et al.* [44] and Walker [45]. A phase-

TABLE VII. Partial χ^2 per data points of π^0 photoproduction for each observable and each laboratory for Solutions I and III.

Solution	$d\sigma/dt$ SLAC [6]	$d\sigma/dt$ DESY [5]	$d\sigma/dt$ DESY [4]	Σ SLAC [6]	Σ GlueX [7]	T Dares [32]	T DESY [33]	P CEA [34]	R_{np} DESY [35]	R_{np} CEA [36]	R_{np} Cornell [37]
I	0.27	1.56	14.5	1.05	4.27	1.69	1.26	2.94	3.85	1.71	1.19
III	0.27	1.36	9.30	4.50	1.05	25.8	4.57	46.2	7.82	3.65	2.82

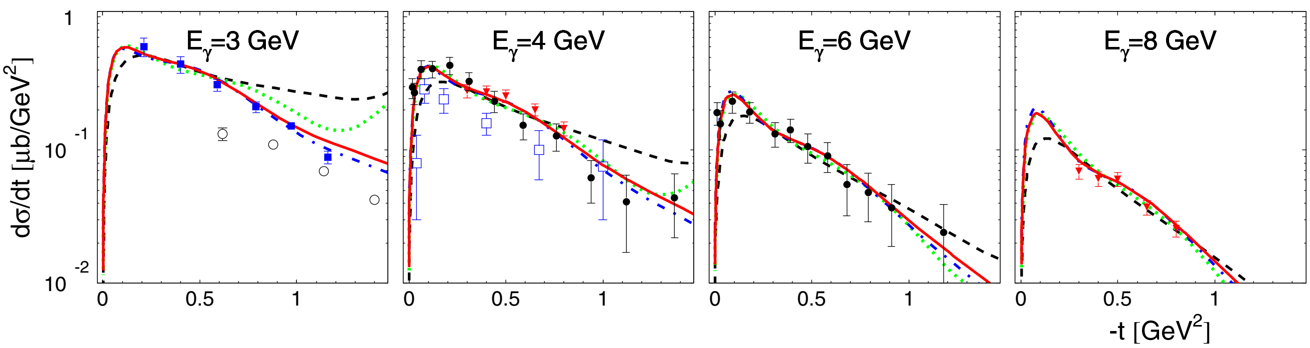

FIG. 8. Differential cross sections for $\gamma p \to \eta p$. The notation of the lines is the same as in Fig. 5. Data: DESY [3] (black disks), WLS [38] (red triangles), Daresbury [40] (blue solid squares), CEBAF Large Acceptnce Spectrometer (CLAS) [41] (black open circles), and CEA [42] (blue open squares).

space factor $|\boldsymbol{q}|/|\boldsymbol{k}|$ has been omitted in all expressions. The differential cross section is given by σ_0 and the spin observables $\check{O}_i$ are obtained from the spin asymmetries A_i by $\hat{O}_i = A_i\sigma_0$:

$$\begin{aligned}
\sigma_0 &= \mathrm{Re}[F_1^*F_1 + F_2^*F_2 + \sin^2\theta(F_3^*F_3/2 + F_4^*F_4/2 \\
&\quad + F_2^*F_3 + F_1^*F_4 + \cos\theta F_3^*F_4) - 2\cos\theta F_1^*F_2],\\
\check{\Sigma} &= -\sin^2\theta\mathrm{Re}[(F_3^*F_3 + F_4^*F_4)/2 + F_2^*F_3 + F_1^*F_4 \\
&\quad + \cos\theta F_3^*F_4],\\
\check{T} &= \sin\theta\mathrm{Im}[F_1^*F_3 - F_2^*F_4 + \cos\theta(F_1^*F_4 - F_2^*F_3) \\
&\quad - \sin^2\theta F_3^*F_4],\\
\check{P} &= -\sin\theta\mathrm{Im}[2F_1^*F_2 + F_1^*F_3 - F_2^*F_4 \\
&\quad - \cos\theta(F_2^*F_3 - F_1^*F_4) - \sin^2\theta F_3^*F_4],\\
\check{E} &= \mathrm{Re}[F_1^*F_1 + F_2^*F_2 - 2\cos\theta F_1^*F_2 \\
&\quad + \sin^2\theta(F_2^*F_3 + F_1^*F_4)],\\
\check{F} &= \sin\theta\mathrm{Re}[F_1^*F_3 - F_2^*F_4 - \cos\theta(F_2^*F_3 - F_1^*F_4)],\\
\check{G} &= \sin^2\theta\mathrm{Im}[F_2^*F_3 + F_1^*F_4],\\
\check{H} &= \sin\theta\mathrm{Im}[2F_1^*F_2 + F_1^*F_3 - F_2^*F_4 \\
&\quad + \cos\theta(F_1^*F_4 - F_2^*F_3)].
\end{aligned}$$

APPENDIX B: CGLN AMPLITUDES IN TERMS OF INVARIANT AMPLITUDES

The CGLN amplitudes are obtained from the invariant amplitudes A_i by the following equations [46,47]:

$$\begin{aligned}
F_1 &= \frac{W - M_N}{8\pi W}\sqrt{(E_i + M_N)(E_f + M_N)} \\
&\quad \times \left[A_1 + (W - M_N)A_4 - \frac{2M_N\nu_B}{W - M_N}(A_3 - A_4)\right],\\
F_2 &= \frac{W + M_N}{8\pi W}|\boldsymbol{q}|\sqrt{\frac{E_i - M_N}{E_f + M_N}} \\
&\quad \times \left[-A_1 + (W + M_N)A_4 - \frac{2M_N\nu_B}{W + M_N}(A_3 - A_4)\right],\\
F_3 &= \frac{W + M_N}{8\pi W}|\boldsymbol{q}|\sqrt{(E_i - M_N)(E_f + M_N)} \\
&\quad \times [(W - M_N)A_2 + A_3 - A_4],\\
F_4 &= \frac{W - M_N}{8\pi W}\boldsymbol{q}^2\sqrt{\frac{E_i + M_N}{E_f + M_N}} \\
&\quad \times [-(W + M_N)A_2 + A_3 - A_4],
\end{aligned}$$

with $\nu_B = (t - \mu^2)/(4M_N)$.

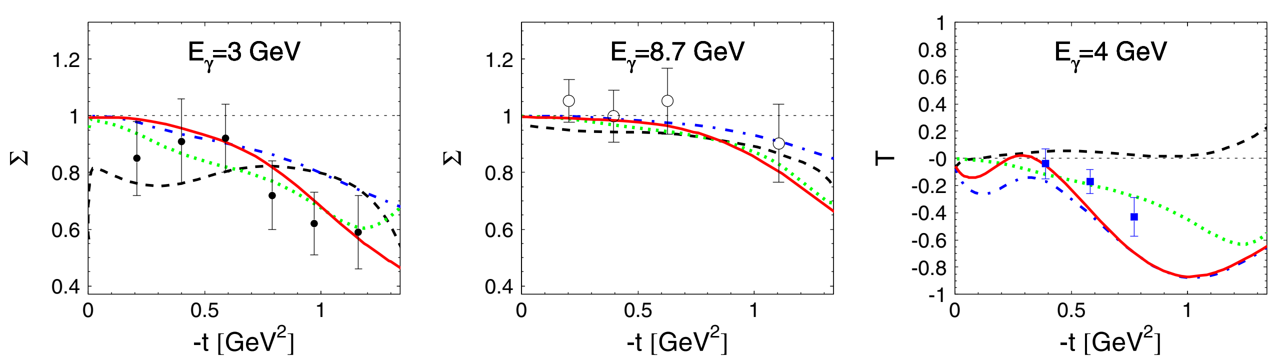

FIG. 9. Polarization observables Σ and T for $\gamma p \to \eta p$. The notation of the lines is the same as in Fig. 5. Data: GlueX [7] (black open circles) and Daresbury: [40] (black disks) and [39] (blue squares).

TABLE VIII. Partial χ^2 per data points of η photoproduction for each observable and each laboratory, for Solutions I and III.

Solution	$d\sigma/dt$ DESY [3]	$d\sigma/dt$ WLS [38]	Σ GlueX [7]	T Daresbury [39]
I	1.05	0.94	0.44	2.94
III	0.98	0.98	0.26	3.80

APPENDIX C: OBSERVABLES IN TERMS OF INVARIANT AMPLITUDES

For high energies, the polarization observables can conveniently be described in terms of invariant amplitudes. Here we follow Ref. [29] and derive the expressions at leading order in the energy squared:

$$\frac{d\sigma}{dt} \approx \frac{1}{32\pi}[|A_1|^2 + |A_2'|^2 - t|A_3|^2 - t|A_4|^2], \quad \text{(C1)}$$

$$\Sigma\frac{d\sigma}{dt} \approx \frac{1}{32\pi}[|A_1|^2 - |A_2'|^2 + t|A_3|^2 - t|A_4|^2], \quad \text{(C2)}$$

$$T\frac{d\sigma}{dt} \approx \frac{1}{16\pi}\sqrt{-t}\,\mathrm{Im}\,[A_1\, A_4^* - A_2'\, A_3^*], \quad \text{(C3)}$$

$$P\frac{d\sigma}{dt} \approx \frac{1}{16\pi}\sqrt{-t}\,\mathrm{Im}\,[A_1\, A_4^* + A_2'\, A_3^*]. \quad \text{(C4)}$$

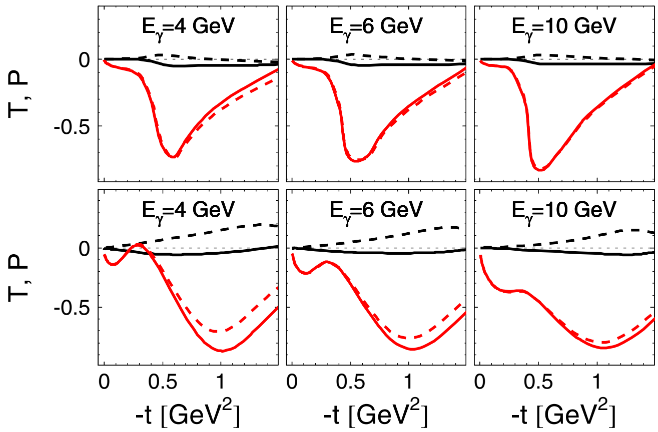

FIG. 10. Comparison of the polarization observables T and P at different photon beam energies for $\gamma p \to \pi^0 p$ (top panels) and for $\gamma p \to \eta p$ (bottom panels). The solid red and black lines are our Solutions I and II for the target polarization T, and the dashed red and black lines are for the recoil polarization P, respectively.

From these relations, a restriction for the difference between target and recoil polarization can be found:

$$|P - T| \leqslant 1 - \Sigma. \quad \text{(C5)}$$

[1] V. Crede and W. Roberts, Rep. Prog. Phys. **76**, 076301 (2013).
[2] A. C. Irving and R. P. Worden, Phys. Rep. **34**, 117 (1977).
[3] W. Braunschweig *et al.*, Phys. Lett. B **33**, 236 (1970).
[4] W. Braunschweig *et al.*, Nucl. Phys. B **51**, 167 (1973).
[5] M. Braunschweig, W. Braunschweig, D. Husmann, K. Lübelsmeyer, and D. Schmitz, Phys. Lett. B **26**, 405 (1968).
[6] R. L. Anderson *et al.*, Phys. Rev. D **4**, 1937 (1971).
[7] H. A. Ghou *et al.* (GlueX Collaboration), Phys. Rev. C **95**, 042201(R) (2017).
[8] I. G. Aznauryan, Phys. Rev. C **67**, 015209 (2003).
[9] I. G. Aznauryan, Phys. Rev. C **68**, 065204 (2003).
[10] B. Pasquini, D. Drechsel, and L. Tiator, Eur. Phys. J. A **27**, 231 (2006).
[11] B. Pasquini, D. Drechsel, and L. Tiator, Eur. Phys. J. A **34**, 387 (2007).
[12] R. Dolen, D. Horn, and C. Schmid, Phys. Rev. **166**, 1768 (1968).
[13] V. Mathieu, I. V. Danilkin, C. Fernández-Ramírez, M. R. Pennington, D. Schott, A. P. Szczepaniak, and G. Fox, Phys. Rev. D **92**, 074004 (2015).
[14] J. Nys, V. Mathieu, C. Fernández-Ramírez, A. N. H. Blin, A. Jackura, M. Mikhasenko, A. Pilloni, A. P. Szczepaniak, G. Fox, and J. Ryckebusch (Joint Physics Analysis Center), Phys. Rev. D **95**, 034014 (2017).
[15] G. F. Chew, M. L. Goldberger, F. E. Low, and Y. Nambu, Phys. Rev. **106**, 1345 (1957).
[16] W. T. Chiang, S. N. Yang, L. Tiator, M. Vanderhaeghen, and D. Drechsel, Phys. Rev. C **68**, 045202 (2003).
[17] M. M. Kaskulov and U. Mosel, Phys. Rev. C **81**, 045202 (2010).
[18] B. G. Yu, T. K. Choi, and W. Kim, Phys. Rev. C **83**, 025208 (2011).
[19] C. Patrignani *et al.* (Particle Data Group), Chin. Phys. C **40**, 100001 (2016).
[20] H. Nagahiro, L. Roca, and E. Oset, Phys. Rev. D **77**, 034017 (2008).
[21] P. D. B. Collins, *An Introduction to Regge Theory and High Energy Physics* (Cambridge University Press, Cambridge, UK, 1977).
[22] A. V. Anisovich *et al.*, Phys. Lett. B **542**, 8 (2002).
[23] A. V. Anisovich *et al.*, Phys. Lett. B **542**, 19 (2002).
[24] S. Godfrey and N. Isgur, Phys. Rev. D **32**, 189 (1985).
[25] G. R. Goldstein, J. F. Owens III, Phys. Rev. D **7**, 865 (1973).
[26] I. S. Barker and J. K. Storrow, Nucl. Phys. B **137**, 413 (1978).
[27] A. Sibirtsev, J. Haidenbauer, S. Krewald, U.-G. Meißner, and A. W. Thomas, Eur. Phys. J. A **41**, 71 (2009).
[28] A. Donnachie and Y. S. Kalashnikova, Phys. Rev. C **93**, 025203 (2016).
[29] V. Mathieu, G. Fox, and A. P. Szczepaniak, Phys. Rev. D **92**, 074013 (2015).
[30] P. V. Landshoff and J. C. Polkinghorne, Phys. Rep. C **5**, 1 (1972).
[31] A. Donnachie, H. G. Dosch, P. V. Landshoff, and O. Nachtmann, *Pomeron Physics and QCD* (Cambridge University Press, Cambridge, UK, 2002).
[32] P. S. L. Booth *et al.*, Phys. Lett. B **38**, 339 (1972).
[33] H. Bienlein *et al.*, Phys. Lett. B **46**, 131 (1973).
[34] M. Deutsch *et al.*, Phys. Rev. Lett. **29**, 1752 (1972); **30**, 249 (1973).
[35] W. Braunschweig *et al.*, Nucl. Phys. B **51**, 157 (1973).
[36] G. C. Bolon, D. Bellenger, W. Lobar, D. Luckey, L. S. Osborne, and R. Schwitters, Phys. Rev. Lett. **27**, 964 (1971).

[37] A. M. Osborne, A. Browman, K. Hanson, W. T. Meyer, A. Silverman, F. E. Taylor, and N. Horwitz, Phys. Rev. Lett. **29**, 1621 (1972); **30**, 814 (1973).

[38] J. Dewire *et al.*, Phys. Lett. B **37**, 326 (1971).

[39] P. J. Bussey *et al.*, Nucl. Phys. B **185**, 269 (1981).

[40] P. S. L. Booth *et al.*, Phys. Lett. B **61**, 479 (1976).

[41] M. Williams *et al.*, Phys. Rev. C **80**, 045213 (2009).

[42] D. Bellenger *et al.*, Phys. Rev. Lett. **21**, 1205 (1968).

[43] A. Sibirtsev, J. Haidenbauer, S. Krewald, and U.-G. Meißner, Eur. Phys. J. A **46**, 359 (2010).

[44] I. S. Barker, A. Donnachie, and J. K. Storrow, Nucl. Phys. B **79**, 431 (1974).

[45] R. L. Walker, Phys. Rev. **182**, 1729 (1969).

[46] P. Dennery, Phys. Rev. **124**, 2000 (1961).

[47] F. A. Berends, A. Donnachie, and D. L. Weaver, Nucl. Phys. B **4**, 1 (1967).